Journal of Ovonic Research Vol. 21, No. 6, November – December 2025, p. 833- 843

Modelling of temperature dependent conduction and filament dynamics in Ag/ZnO/FTO memristor

S. Panda[a], C. S. Dash[a,*]
[a] *Department of Electronics and Communication Engineering, Centurion University of Technology and Management, Odisha, Bhubaneswar, 752050, India*

This work presents a mathematical model describing the resistive switching behavior in Ag/ZnO/FTO memristor. Further, analyses are employed to distinguish the active conduction mechanisms in different bias regimes and simultaneously a hybrid mathematical model is developed that combines Schottky type interfacial injection, Poole Frenkel (PF) bulk emission, and Ohmic filament conduction, with a logistic state variable describing filament formation and rupture. Furthermore, the model is implemented in MATLAB, and nonlinear fitting of the experimental sweeps demonstrated excellent agreement between simulation and measurement. Extracted parameters such as ON and OFF state resistances (R_{on} and R_{off}), barrier height ($\emptyset_B$) and ionic mobility (μ_{ion}) provide insights into conduction dynamics, confirming filamentary electrochemical growth as the dominant switching mechanism in ZnO based memristors. Moreover, the study considers temperature dependent rupture dynamics, where the exponential thermal activation factor is proportional to the existing filament, with filament formation in the proposed memristor being primarily field driven but enhanced by temperature through increased ionic mobility.

(Received September 25, 2025; Accepted December 16, 2025)

Keywords: Resistive switching, Ag/ZnO/FTO device, Filament dynamics, Conduction mechanisms, Temperature dependence, Bipolar I–V characteristics.

1. Introduction

The continuous demand for energy-efficient, high-density, and non-volatile memory devices has driven significant research into next-generation memory technologies that can overcome the limitations of conventional Complementary Metal Oxide Semiconductor (CMOS)-based architectures. Among the emerging alternatives, resistive random-access memory (RRAM) based on memristive devices has attracted widespread attention due to its simple metal-insulator-metal (MIM) structure, low power consumption, fast switching speed, and potential for neuromorphic computing applications [1]. Further, in a memristor, resistance changes dynamically in response to applied voltage or current, providing non-volatile storage and memory functions [2]. Such devices inherently combine memory and processing functions, enabling non-Von Neumann architectures that are better suited for brain-inspired computing paradigms.

Metal oxides, particularly transition-metal oxides, have emerged as promising switching materials for memristive devices because of their tunable defect chemistry, thermal stability, and compatibility with silicon-based fabrication [3]. Among these oxides, zinc oxide (ZnO) has been extensively studied due to its wide bandgap (3.37 eV), high exciton binding energy (60 meV), chemical stability, and the ability to tune oxygen vacancy concentration through doping and processing conditions [4]. Importantly, ZnO based devices have demonstrated reproducible resistive switching characteristics with large ON/OFF ratios, making them attractive candidates for both memory and neuromorphic applications.

* Corresponding author: chandu0071@gmail.com
https://doi.org/10.15251/JOR.2025.216.833

Schottky emission at the metal/semiconductor interface or bulk-limited mechanisms such as Poole Frenkel (PF) emission and space-charge-limited current (SCLC) related to trap states in the oxide [5]. At higher voltages, electrochemical processes drive the migration of oxygen vacancies or metal ions, producing conductive filaments within the oxide. This filamentary conduction leads to a sharp current increase and transition into the low resistance state (LRS). Filament rupture under reverse bias or Joule heating resets the device to the high resistance state (HRS) [6]. The coexistence of interfacial and filamentary conduction necessitates hybrid models that capture both contributions for accurate device representation. Diagnostic methods help distinguish these mechanisms: Ohmic conduction appears as a slope of unity in log-log I–V plots, while SCLC shows quadratic or higher-order dependence. Schottky emission is verified by linearity in $\ln(J/T^2)$ vs. $\sqrt{E}$ plots, yielding barrier information, while PF conduction is confirmed by $\ln(J/E)$ vs. $\sqrt{E}$ linearity, indicating trap-assisted bulk transport [7].

Mathematical modelling of memristors links experimental observations to physical mechanisms and enables parameter extraction for optimization [8]. Early models, such as Strukov *et al.*, described memristance via ionic drift and ON/OFF resistance interpolation but failed to capture nonlinear switching and multiple conduction paths. Advanced models use logistic state variables and window functions to constrain filament growth and rupture [9]. In ZnO, hybrid models combining Schottky or PF conduction with filamentary Ohmic paths replicate I–V hysteresis. The Ag/ZnO/FTO device [10] shows bipolar ±1 V switching as illustrated in Fig. 1, with Schottky-like rectification and filamentary conduction, modelled effectively using hybrid approaches. In this work for the first time a physics based model is proposed which explains the filamentary conduction in ZnO based memristor and further exaplains the impact of temperature on the process of formation and rupture of conducting filaments which is a widely accepted phenomenon responsible for Resistive switching.

The present work is organized as follows. In Section 2, the mathematical modelling of Ag/ZnO/FTO is discussed and in Section 3, model fitting parameters of experimental observations are obtained. In Section 4 the temperature dependence is considered whereas in Section 5, the effect of temperature on I–V characteristics is observed. Additionally, in Section 6 the conclusion along with further perspectives are illustrated.

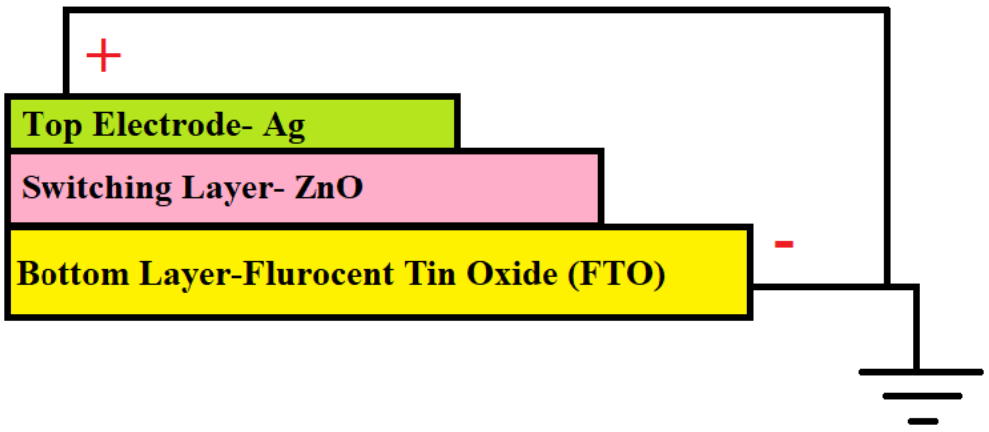

Fig. 1 . Device structure representing Ag/ZnO/FTO.

2. Mathematical modelling of Ag/ZnO/FTO

As noted by Pradhan *et al*. [10] the experimental evaluations for Ag/ZnO/FTO based memristive device were conducted under standard laboratory ambient conditions at room temperature, where during the electrical measurements, a bias voltage was applied to the top Ag

electrode while maintaining the FTO bottom electrode at ground potential. The I–V characteristics were systematically acquired through a voltage sweep in the range of ±1 V, with a fixed step increment of 0.01 V. The typical I–V response, as illustrated by the Fig. 2. [10], reveals that the Ag/ZnO/FTO structure exhibits reversible switching at both positive and negative polarities, thereby indicating the manifestation of a bipolar resistive switching (RS) mechanism. In the present work, the mathematical modelling is demonstrated to accurately fit the experimental measurements [10].

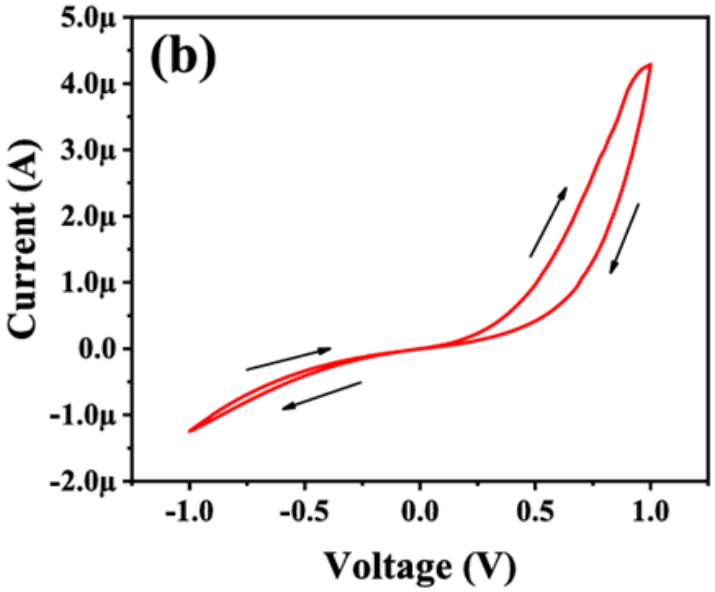

Fig. 2. Single I-V curve of Ag/ZnO/FTO (Reprinted with permission from Ref. [10]).

The device demonstrates a hybrid conduction behavior in which both interfacial and filamentary mechanisms contribute to the observed I–V characteristics [10-12]. At low voltages, the transport is dominated by electrode-limited or trap-assisted mechanisms such as Schottky emission, Poole Frenkel (PF), or space-charge-limited current (SCLC), while at higher voltages beyond a threshold the conduction is governed primarily by the formation of metallic filaments inside the ZnO switching layer [4, 13]. This hybrid picture is consistent with other studies on ZnO based resistive switching, where interface limited injection dominates in the high resistance state (HRS) and filamentary conduction governs the low resistance state (LRS) [1, 14].

From a physical perspective as shown in Fig. 3, the pre-SET regime (HRS), at very low biases the current follows Ohmic conduction ($I \propto V$), after which Schottky emission at the Ag/ZnO interface becomes significant. Trap-assisted mechanisms such as PF emission or trap-controlled SCLC contribute depending on defect concentration, electrode work function, and film thickness [5, 15]. Once the applied field reaches a threshold, ion migration (Ag^+ or oxygen vacancies) initiates filament nucleation and growth, leading to a sharp transition to the LRS. After SET, conduction is dominated by Ohmic transport through the metallic filament, typically expressed as $I \approx V/R_{on}$. During the RESET process, the filament ruptures by Joule heating, ionic diffusion and electrochemical oxidation, resulting in a return to HRS [9, 16]. Diagnostic linearization helpsdistinguish between conduction mechanisms. Ohmic conduction appears as a slope of unity in I–V plot. SCLC manifests as a quadratic dependence ($I \propto V^2$) in trap-free conditions or with higher slopes in trap-filled regimes. Schottky emission can be verified by plotting ln (J/T^2) versus $\sqrt{E}$, yielding a straight line from which barrier height ($\emptyset_B$) can be extracted. Here $J = I/A_e$ is the current density, A_e is the electrode area, T represents the temperature, $E = V/D$ is the electric field and D represents the thickness of ZnO switching layer. PF conduction is instead tested by plottingln (J/T^2) versus $\sqrt{E}$ and linearity in this plot indicates bulk trap-assisted emission. These

diagnostics have been applied extensively in ZnO resistive switching devices to identify the dominant mechanism in each regime [7, 17].

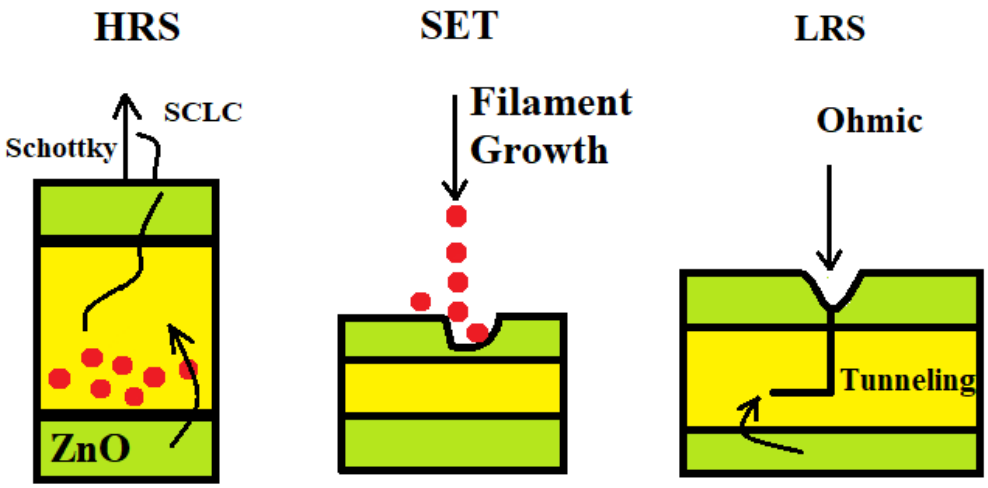

Fig. 3 . Diagnostic diagrams for identifying conduction mechanisms in ZnO memristors, including Ohmic conduction, Schottky emission and SCLC. HRS, high resistance state; SET, separated into forward; LRS, low resistance state.

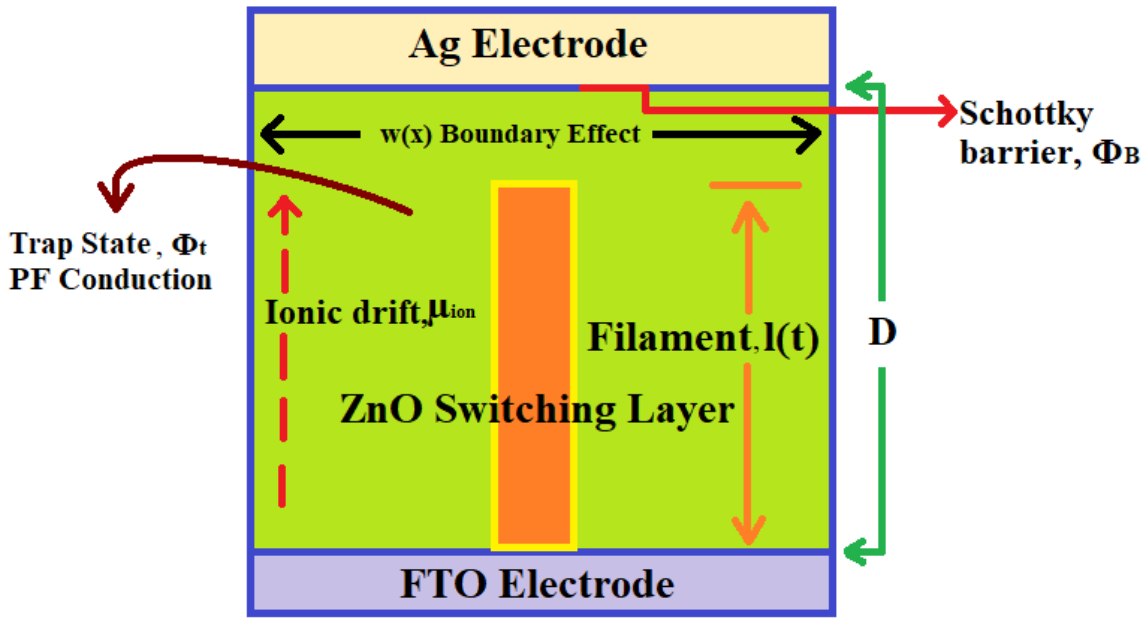

Fig. 4. Schematic of Ag/ZnO/FTO memristor showing device layers and filament dynamics.

To model these processes, it is essential to introduce a set of key parameters. The device thickness (D) and electrode area (A_e) define the internal electric field and current density. The ON- and OFF-state resistances (R_{on} and R_{off}) represent conduction through the metallic filament and pristine ZnO matrix, respectively. The state variable $x(t)$ governs the interpolation between HRS

and LRS. Ionic mobility (μ_{ion}) controls filament dynamics, while conductivity (σ) and relative permittivity (ε_r) affect bulk transport. Schottky barrier height ($\emptyset_B$) and and trap depth ($\emptyset_t$) determine injection and PF conduction, respectively as illustrated in Fig. 4. Additional terms such as tunnelling factor (I_0) and attenuation coefficient (α) capture pre-bridging tunnelling currents. Window functions ($w(x)$) are necessary to constrain x within [0,1] and model boundary effects near electrodes [18]. In this context, the physics based mathematical model can be expressed as follows:

By Using the Schottky emission,

$$J_S = A^* T^2 \exp\left(-\frac{q\emptyset_B - \beta_S\sqrt{E}}{kT}\right) \qquad (1)$$

Where J_S is the current density, A^* is the Richardson constant originates from thermionic emission theory and represents the material-specific factor in the current density equation. The term A^*T^2 represents the carrier supply function at temperature T. k is the Boltzmann's constant and q represents the charge of an electron. β_S is the interface effect (Schottky barrier lowering coefficient) [7, 19]. The experimental device shows rectifying behaviour consistent with Schottky at Ag/ZnO.

$$J_{PF} \propto Ee^{-\frac{q\emptyset_t - \beta_{PF}\sqrt{E}}{kT}} \qquad (2)$$

Where J_{PF} is the current density, $\emptyset_t$ is the trap depth energy level (eV) for PF and β_{PF} is the PF barrier lowering coefficient has the same origin as Schottky lowering, but it applies to bulk trap states. A linear fit indicates Schottky as well as PF, but the test electrode changes (Schottky is electrode-limited, and PF is bulk-limited). $x(t)$ is the dynamical state of the memristor and modelling with $x(t)$ captures hysteresis [20]. It is given by

$$x(t) = l(t)/D, \qquad 0 \le x \le 1 \qquad (3)$$

The total conduction in a memristor can be thought of as two parallel paths, a bulk ZnO path (insulating matrix) and a filamentary metallic path (conductive channel). Further, the effective memristance is obtained by combining them with a state variable.

$$R(x) = R_{on}.x + R_{off}.(1-x) \qquad (4)$$

The memristance, $R(x)$ is the weighted average [21] between R_{on} and R_{off} with $x \in (0,1)$. Now, to know about the internal state variable changes with time, the rate of change of normalized filament length can be written as

$$\frac{dx}{dt} = \mu_{ion}\frac{V_{int}}{D}w(x) - \Gamma e^{-E_a/kT} g\,(x,I,T) \qquad (5)$$

Where $g\,(x,I,T)$ is a rupture function and it describes how the existing filament decays (ruptures) under current and temperature, E_a represents the activation energy barrier for rupture (eV) controlling how strongly rupture depends on temperature and Γ is the rupture kinetics pre-factor.V_{int} is the effective internal voltage across the switching layer accounting for voltage division across filaments. Moreover, the filament kinetics which are the filament formation and rapture can be observed from equation (5) is a differential equation. Here, $\mu_{ion}\frac{V_{int}}{D}\,w(x)$ is field driven ionic drift and $\Gamma e^{-E_a/kT} g\,(x,I,T)$ is thermally activated. $w(x)$ is a window function, a Biolek current dependent form to show motion near boundaries and polarity sensitivity in the boundary dynamics [22].

Furthermore, in case of slowly varying V, approximate steady-state growth balance and treat x as a monotonic function of V. Here, $dx/dt = 0$ for each sweep point to obtain $x(V)$.

$$x(V) = \frac{1}{1+\exp\left(-\frac{V-V_{th}}{\Delta V}\right)} \qquad (6)$$

Where V_{th} is the SET threshold voltage and ΔV controls steepness, which is also linked to μ_{ion} and Γ. Equation (6) is an empirical approximation to achieve a closed form for $I(V)$.

The total current is the sum of bulk electrode or trap current, Ohmic filament conduction current and the tunnelling current, hence,

$$I(V,x) = I_{bulk}(V).[1 - H(x - x_c)] + \frac{V}{R(x)} + I_{tun}(V, D(1-x)) \qquad (7)$$

Where the bulk conduction term, $I_{bulk}(V)\,.\,[1-H(x-x_c)]$ represents a non-filamentary Schottky, PF and SCLC transports. $I_{bulk}(V)$ is active when $x < x_c$. The Heaviside function $H(x-x_c)$ with x_c as a critical threshold value of x at which the filament is considered to bridge the device and form a low-resistance path, switches this contribution off once the filament bridges. Further, when the filament exists, the current flows through it and the Ohmic current is represented by $V/R(x)$.

For bulk model in terms of Schottky transport,

$$I_S(V) = A_e A^* T^2 \exp\left(-\frac{q\emptyset_B - \beta_S\sqrt{E}}{kT}\right) \text{ with } \beta_S = \sqrt{\frac{q^3}{4\pi\varepsilon_r\varepsilon_0}} \quad (8)$$

For bulk model in terms of PF transport,

$$I_{PF}(V) = C\,E\,\exp\left(-\frac{q\emptyset_t - \beta_{PF}\sqrt{E}}{kT}\right) \quad \text{with} \quad \beta_{PF} = \sqrt{\frac{q^3}{\pi\varepsilon_r\varepsilon_0}} \quad (9)$$

When the filament is close to bridging, the tunnelling current between the filament tip and counter electrode can be represented as

$$I_{tun}(V,x) = I_0(V)\exp(-\alpha D(1-x)) \quad \text{with} \quad \alpha \propto \sqrt{\frac{(2m^*\emptyset_B)}{h^2}} \quad (10)$$

Where α is the attenuation coefficient of the tunnelling wavefunction inside the barrier, m^* is $0.24m_0$ with m_0 is the free electron mass, called effective electron mass in ZnO, $I_0(V)$ is pre-exponential factor or tunnelling factor and h is the Plank's constant.

3. Model fitting

The fitting workflow begins with the preprocessing of the experimental I–V sweeps. The raw curve should be separated into forward (SET) and reverse (RESET) branches. Resistances R_{on} and R_{off} are estimated directly from the low-bias slopes in the LRS and HRS regions, respectively. Plots based on Schottky and PF analysis are then applied to identify which conduction mechanism dominates in the HRS. For experimental work, Schottky emission at the Ag/ZnO interface is the most consistent with the rectifying behavior and linearization results, while PF may contribute weakly [10, 23].

In the fitting stage, nonlinear least squares methods are employed. The hybrid model equations described above are implemented with various parameters and the fitting is performed separately on the SET and RESET conditions to capture asymmetry. Additionally, parameter constraints are set using physical estimates [24]. The quality of the fit is evaluated by comparing the modelled and experimental I–V curves on linear and logarithmic scales, and by analyzing residuals. The fitted parameters provide insight into the physical processes such as a lower extracted R_{on} corresponds to stronger metallic conduction, while a higher R_{off} reflects trap-assisted leakage [25]. The barrier height $\emptyset_B$ and attenuation coefficient α reveal the relative contribution of interfacial vs. tunnelling processes. Moreover, the transition parameters V_{th} and ΔV quantify the threshold behavior and sharpness of filament formation, respectively [25-27].

3.1. Approximations and scaling relations

In practical modelling of ZnO based memristors, several useful closed-form expressions and scaling relations allow parameter extraction directly from experiments. The switching time for SET can be approximated using ionic drift as

$$t_{set} \approx \frac{D}{\mu_{ion}E} = \frac{D^2}{\mu_{ion}V} \Rightarrow \mu_{ion} = \frac{D^2}{Vt_{set}} \quad (11)$$

This relation is widely used to estimate μ_{ion} from measured switching times. The ON- and OFF-state resistances can be estimated from small-signal read operations as

$$R_{on} \approx \frac{V_{read}}{I_{LRS}}\,,\, R_{off} \approx \frac{V_{read}}{I_{HRS}} \quad (12)$$

Where V_{read} is a low, non-disturbing read voltage, and I_{LRS}, I_{HRS} are the measured currents in low and high resistance states respectively. For Schottky emission, the slope in a linearized plot ofln (J/T^2) versus $\sqrt{E}$ provides

$$m_s = \frac{q}{kT}\left(\frac{q}{4\pi\varepsilon_r\varepsilon_0}\right)^{1/2} \quad (13)$$

This scaling relation helps assess whether Schottky emission is the dominant mechanism by comparing experimental slopes with theoretical values [28]. Collectively, these approximations provide initial estimates for key physical parameters.

3.2. Parameter dependent effects on resistive switching and filamentary behavior

The conduction behavior and resistive switching performance of ZnO based memristors are strongly influenced by variations in their physical key parameters [7, 29]. μ_{ion} dictates the rate of filament formation, where higher values accelerate the SET process but may lead to unstable or residual filaments. R_{on} and R_{off} determine the current levels in the low and high resistance states, thereby defining the switching ratio and energy consumption. σ affects the ease of charge transport [4], [5, 30]. ε governs barrier lowering in Schottky and PF conduction. $\emptyset_B$ controls electron injection at the electrode interface and $\emptyset_t$ influences PF and SCLC mechanisms, impacting leakage in the HRS.

3.3. Proposed hybrid expression for accurate I–V representation

By utilizing the logistic function in equation (6) for $x(V)$ together with the composite current model in equation (7), incorporating the Schottky bulk conduction in equation (8) and tunnelling contribution in equation (10), the combination yields a practical three-term fitting expression suitable for accurately reproducing the experimental I–V characteristics.

$$I(V) = I_S(V)\big(1 - S(x)\big) + \frac{V}{R_{off}(1-x)+R_{on}x} + I_0\exp\left(-\alpha D(1-x)\right) \quad (14)$$

where, $S(x) = \frac{1}{2}[1 + \tanh\left(k(x - x_c)\right)]$ is a smooth transition function and moves the contribution from bulk to filament smoothly. Instead of cutting bulk conduction off suddenly, it gradually reduces bulk contribution while gradually increasing filament contribution as x approaches x_c.

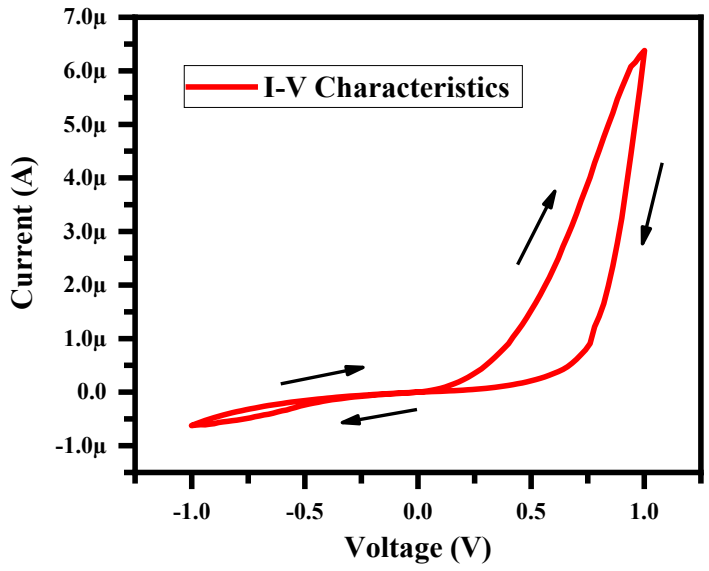

Fig. 5. Proposed single I–V representation obtained by analysis fit with the experimental representation.

The plots in Fig. 2 [10] and Fig. 5 exhibit bipolar resistive switching with a distinct SET process at positive bias and RESET transition under reverse bias, accompanied by hysteresis consistent with filament formation and rupture. The simulated curve in Fig. 5 successfully reproduces the sharp current increase during SET, the rectifying nature at low bias, and the transition between HRS and LRS. Furthermore, the variation of current in the μA range with respect to the same applied voltage closely matches in both plots, validating the suitability of the developed model. Hence, the present work confirms that the proposed mathematical model achieves successful fitting with the experimental data.

4. Temperature dependency of the proposed modified mathematical model

Temperature, T enhances ionic drift and filament formation but also accelerates filament rupture via thermally activated diffusion and oxidation. From equation (8) it can be observed the T^2 prefactor and$\exp\left(-\frac{q\emptyset_B}{kT}\right)$ show that Schottky current increases with T. The growth term depends on μ_{ion}, which itself increases with T, indication faster movement of ions, can be seen in equation (5). Further, the rupture is exponentially faster at higher T. These conditions make $x(V)$ explicitly temperature dependent. Additionally, at higher T, more electrons have enough energy above the Fermi level to participate in tunnelling. This increases the supply of tunnelling electrons, hence I_0 rises slightly with T. Substituting these factors into equation (14) the modified temperature dependent I-V relationships can be written as

$$I(V) = A_e A^* T^2 \exp\left(-\frac{q\emptyset_B - \beta_S\sqrt{E}}{kT}\right)\left(1 - S(x)\right) + \frac{V}{R\left(x(V,T)\right)} + I_0(V,T)\left(\exp(-\alpha D(1-x)\right) \quad (15)$$

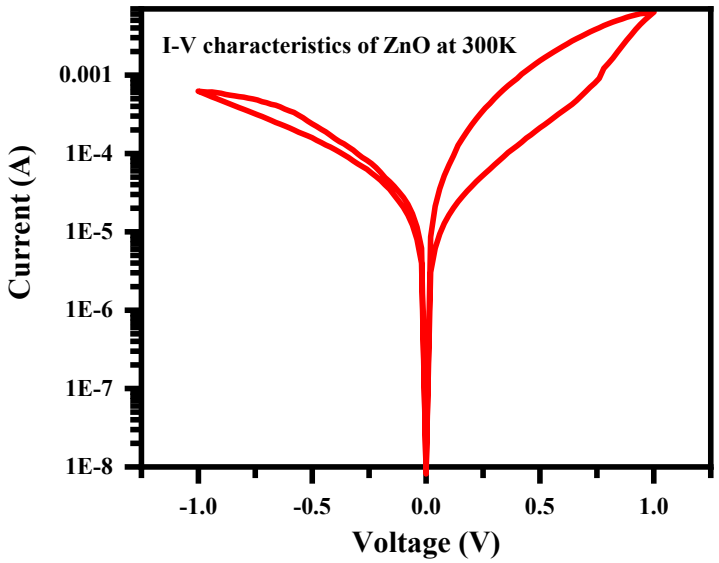

Fig. 6. Proposed I–V characteristics at 300K.

The temperature dependent I–V characteristic is modelled using equation (15) and is shown in Fig. 6, which incorporates Schottky emission, filament dynamics, and tunnelling with explicit

thermal activation. The proposed temperature-dependent model is simulated at 300 K, showing consistency with the experimental behavior of the Ag/ZnO/FTO device.

5. Effect of temperature on I-V characteristics

Implementing the temperature dependence study at higher T, Schottky term grows, filament forms with ruptures at a faster rate and more thermal carriers are available with a slightly increase in tunnelling. Thus, the I–V curve shifts to higher current in HRS and shows faster SET and RESET dynamics. In this context, the temperature dependent I–V curves were measured at 300 K, 350 K, and 400 K as illustrated in Fig. 7.

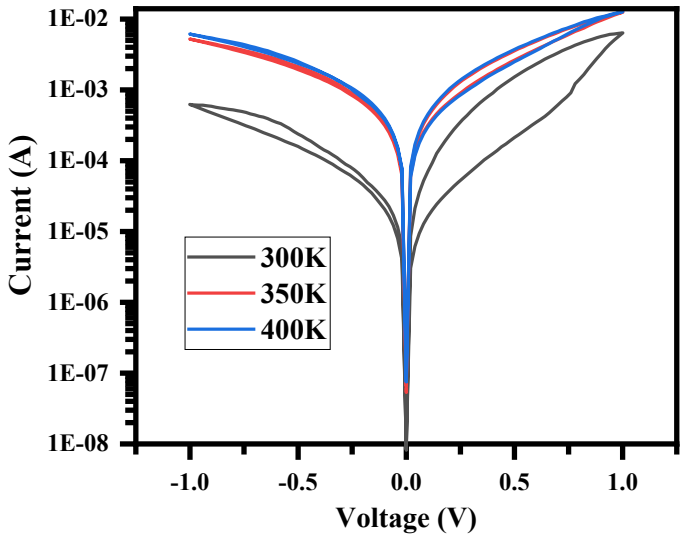

Fig. 7. The effect of temperature on the current based on the proposed mathematically fit model at 300K, 300K and 400K.

A comparative analysis is made with the calculated values of $\left({R_{on}}/{R_{off}}\right)$, μ_{ion} and Memristance at various temperatures (300 K to 400 K) are presented in Table 1. μ_{ion} increases with T due to thermally activated ionic migration. Further, memristance rises with an increase in temperature and the HRS to LRS ratio $\left({R_{off}}/{R_{on}}\right)$ remains relatively stable because both HRS and LRS vary with temperature at nearly equal rates. A larger HRS to LRS ratio indicates better contrast between ON and OFF states, thereby easier to read data reliably.

Table 1. Performance of the model at different temperatures.

T(K)	μ_{ion}(m^2/V. s)	${R_{off}}/{R_{on}}$	Memristance (Ω)
300	3.984×10^{-21}	1.224×10^{6}	1.045×10^{6}
350	6.314×10^{-20}	0.995×10^{6}	1.816×10^{6}
400	5.015×10^{-19}	1.09×10^{6}	2.148×10^{6}

6. Conclusions

In this work, the electrical characteristics of the Ag/ZnO/FTO memristor were systematically analyzed and successfully fitted using a physics-based mathematical model. Experimental I–V measurements revealed bipolar resistive switching with well-defined SET and RESET processes, governed by a combination of Schottky emission, Poole Frenkel conduction, SCLC, and filamentary Ohmic transport. By incorporating key parameters such as device thickness, ionic mobility, conductivity, barrier height, trap depth, and temperature dependence, a hybrid model was developed that closely reproduces the experimental hysteresis. The inclusion of logistic state variables and window functions enabled an accurate description of filament growth and rupture, while tunnelling contributions captured pre-SET leakage. Comparison between experimental and simulated plots demonstrated excellent agreement, with current variation in the μA range closely matching across voltage sweeps. Furthermore, the temperature-dependent formulation provides a framework to evaluate thermal effects on filament dynamics. Overall, the model fitting validates the proposed approach and provides meaningful parameters for device optimization. Future work will extend this framework to develop SPICE models and integtrate this CMOS technology to develop novel circuits based on Hybrid CMOS- Memristor technologies.

Acknowledgments

Authors are thankful to the management of Centurion University of Technology and Mangement, Odisha for providing the requisite support to undertake this research work.

Conflict of interest

The authors declare no conflict of interest.

References

[1] H. Abunahla, B. Mohammad, Memristor Technology: Synthesis and Modeling for Sensing and Security Applications, Springer International Publishing, Cham 93(2017).
[2] T. Guo, K. Pan, Y. Jiao, B. Sun, C. Du, J. P. Mills, Z. Chen, X. Zhao, L. Wei, Y. N. Zhou, Y. A. Wu, Nanoscale Horizons **7**(3), 299 (2022).
[3] M. Lübben, F. Cüppers, J. Mohr, M. von Witzleben, U. Breuer, R. Waser, C. Neumann, I. Valov, Science Advances **6**(19), eaaz9271 (2020). https://doi.org/10.1126/sciadv.aaz9271
[4] M. Ismail, M. Rasheed, C. Mahata, M. Kang, S. Kim, Journal of Alloys and Compounds **960**, 170464 (2023). https://doi.org/10.1016/j.jallcom.2023.170464
[5] F. Gul, H. Efeoglu, Ceramics International **43**(14), 10770 (2017). https://doi.org/10.1016/j.ceramint.2017.05.341
[6] T. Li, H. Yu, S. H. Y. Chen, Y. Zhou, S. T. Han, Journal of Materials Chemistry C **8**(46), 16295 (2020). https://doi.org/10.1039/D0TC03378F
[7] R. J. Gray, Memristor-Based Materials and Devices for Neuromorphic Computing, Doctoral Dissertation, University of Hull (2017).
[8] S. Panda, C. S. Dash, R. Jothiramalingam, H. Al-Lohedan, Journal of Ovonic Research **20**(3), 123 (2024).
[9] A. Mazady, Memristor: Part I—The Underlying Physics and Conduction Mechanism, Doctoral Dissertation, University of Notre Dame (2014).
[10] S. K. Pradhan, S. A. Ahir, T. D. Dongale, J. R. Rajabathar, S. Sasikumar, S. Chakravarty, C. S. Dash, R. Balu, Journal of Materials Science: Materials in Electronics **36**(25), 1 (2025). https://doi.org/10.1007/s10854-025-12345-6
[11] L. Wang, C. H. Yang, J. Wen, S. Gai, Y. X. Peng, Journal of Ovonic Research **11**(3), 145 (2015).
[12] A. N. Busygin, S. Y. Udovichenko, A. H. A. Ebrahim, A. N. Bobylev, A. A. Gubin, physica status

solidi (a) **220**(11), 2300123 (2023). https://doi.org/10.1002/pssa.202300123
[13] S. Gora, L. Thyda, G. Dasi, R. Muniramaiah, A. Thakre, J. Gangwar, D. P. Joseph, M. Kovendhan, P. A. Azeem, D. Dinakar, K. Thangaraju, Surfaces and Interfaces **30**, 101950 (2022). https://doi.org/10.1016/j.surfin.2022.101950
[14] K. Jagannadham, Applied Physics A **127**(4), 285 (2021). https://doi.org/10.1007/s00339-021-04367-2
[15] J. Wang, B. Sun, G. Zhou, S. Zhu, C. Yang, C. Ke, Y. Zhao, H. Wang, Journal of Alloys and Compounds **939**, 168726 (2023). https://doi.org/10.1016/j.jallcom.2023.168726
[16] G. Zhang, J. Qin, Y. Zhang, G. Gong, Z. Y. Xiong, X. Ma, Z. Lv, Y. Zhou, S. T. Han, Advanced Functional Materials **33**(42), 2304192 (2023). https://doi.org/10.1002/adfm.202304192
[17] K. Kumari, S. Majumder, A. D. Thakur, S. J. Ray, Materials Letters **303**, 130451 (2021). https://doi.org/10.1016/j.matlet.2021.130451
[18] Z. Biolek, D. Biolek, V. Biolkova, Radioengineering **18**(2), 210 (2009).
[19] F. Yan, Y. Wang, J. Zhang, Z. Lin, J. Zheng, F. Huang, ChemSusChem **7**(1), 101 (2014). https://doi.org/10.1002/cssc.201301327
[20] A. Zaman, Memristor Devices for Neuromorphic Computing, Doctoral Dissertation, University of Dayton (2020).
[21] O. G. Kharlanov, B. S. Shvetsov, V. V. Rylkov, A. A. Minnekhanov, Physical Review Applied **17**(5), 054012 (2022). https://doi.org/10.1103/PhysRevApplied.17.054012
[22] V. Mladenov, S. Kirilov, Electronics **6**(4), 77 (2017). https://doi.org/10.3390/electronics6040077
[23] P. S. Huang, F. Qin, J. K. Lee, ACS Applied Materials & Interfaces **12**(4), 4715 (2020). https://doi.org/10.1021/acsami.9b18123
[24] F. Ouaja Rziga, K. Mbarek, S. Ghedira, K. Besbes, Applied Physics A **123**(4), 288 (2017). https://doi.org/10.1007/s00339-017-0902-9
[25] E. Gale, B. de Lacy Costello, A. Adamatzky, Proceedings of the IEEE International Conference on Electronics Design, Systems and Applications (ICEDSA) **2012**, 80 (2012). https://doi.org/10.1109/ICEDSA.2012.6507822
[26] J. D. H. Zesch, Memristor Modeling and Applications in Neuromorphic Systems, Doctoral Dissertation, Stanford University (2024).
[27] P. J. Skrodzki, M. Burger, I. Jovanovic, Scientific Reports **7**(1), 370 (2017). https://doi.org/10.1038/s41598-017-00470-5
[28] A. Ruzin, Journal of Applied Physics **118**(20), 204502 (2015). https://doi.org/10.1063/1.4936590
[29] K. M. Kim, M. H. Lee, G. H. Kim, S. J. Song, J. Y. Seok, J. H. Yoon, C. S. Hwang, Applied Physics Letters **97**(16), 162912 (2010). https://doi.org/10.1063/1.3505114
[30] S. Dirkmann, J. Kaiser, C. Wenger, T. Mussenbrock, ACS Applied Materials & Interfaces **10**(17), 14857 (2018). https://doi.org/10.1021/acsami.7b19925

.